Sustainable Energy & Fuels

ROYAL SOCIETY OF CHEMISTRY

PAPER

View Article Online
View Journal | View Issue

Cite this: *Sustainable Energy Fuels*, 2022, **6**, 2858

A solution-processed MoS_2/graphene heterostructure mediated by a bifunctional block copolymer as a non-noble metal platform for hydrogen evolution†

Andriana Plantzopoulou,[a] Ioanna K. Sideri, ‡[a] Anastasios Stergiou, ‡[a] Martha Kafetzi,[a] Stergios Pispas, *[a] Raul Arenal *[bcd] and Nikos Tagmatarchis *[a]

Development of synthetic strategies towards two-dimensional laminar transition metal dichalcogenide/graphene heterostructures is of particular interest for the electrocatalytic hydrogen evolution reaction (HER). Herein, we describe the preparation of a molybdenum disulfide/graphene heterostructure, mediated by a bifunctional polystyrene-*b*-poly(acrylic acid) block copolymer. Surface engineering of graphene nanosheets by incorporation of ammonium-terminated organic chains facilitated attractive electrostatic interactions with the anionic polycarboxylate block of the copolymer, while the phenyl rings of the polystyrene block of the copolymer enabled the development of multiple van der Waals π–S interactions with the surface sulfur atoms of MoS_2. The heterostructure exhibits excellent HER performance, as a result of the synergistic effect of 1T-MoS_2 loading onto graphene and the latter's charge delocalization efficiency. An onset overpotential value of −0.18 V *vs.* RHE, a small charge transfer resistance of 36.2 Ω and a large electrocatalytic surface area of 205 cm^2 were obtained, paving the way for the construction of advanced heterostructures based on graphene and transition metal dichalcogenides with improved electrocatalytic activity.

Received 17th February 2022
Accepted 2nd May 2022

DOI: 10.1039/d2se00218c

rsc.li/sustainable-energy

Introduction

Isolation of graphene nanosheets from natural graphite[1] boomed the interest in environmentally stable two-dimensional (2D) nanostructures. Later on, the emergence of graphene modified analogues and hybrids paved the way for the dominance of the graphene family of materials in multiple applications such as optoelectronics and photocatalysis, among others.[2] Furthermore, their chemical and electronic coupling effects along with their high conductivity and charge transport are responsible for their advanced performance in catalysis,[3] nanoelectronics[4] and energy storage-related applications.[5] Their increased stability in a wide range of pH as well as their large specific surface area greatly support their utilization as a substrate/support system for the immobilization of transition metal dichalcogenides (TMDs), enabling their excellence in other domains as well, such as electrocatalysis. In particular, the hybridization of graphene analogues with molybdenum disulfide (MoS_2) for example, the most-studied member of the family of TMDs, unveiled new ventures in hydrogen evolution reaction (HER) electrocatalysis, due to the synergistic effect of graphene charge transport and MoS_2 catalytically active sites.[6]

The superiority of 1T (metallic and octahedral) *versus* 2H (semiconducting and trigonal prismatic) polytype of MoS_2 with respect to the HER is well-known,[7,8] and arguably, the research interest is now primarily oriented to derivatives with enhanced 1T-MoS_2 phases, holding the prominence as one of the best earth-abundant HER electrocatalysts. Although 1T-MoS_2 shows intrinsic elevated electrocatalytic activity for the HER, owing to its exposed abundant sulfur edges at the periphery[9] and to the scarce unsaturated Mo atoms of the basal plane,[10] there is still room to further ameliorate its performance based on certain characteristics. Relatively lower conductivity, potential aggregation, thermodynamic instability of the 1T phase and the catalytically inert/scarcely activated basal plane of the material are some of these characteristics. To this end, efforts have been made to increase the active sites, their electrical contact, the mass and electron transfer and the specific surface area of the material by interfacing MoS_2 with graphene-related materials.

[a]*Theoretical and Physical Chemistry Institute, National Hellenic Research Foundation, 48 Vassileos Constantinou Avenue, Athens 11635, Greece. E-mail: tagmatar@eie.gr*
[b]*Laboratorio de Microscopias Avanzadas (LMA), Universidad de Zaragoza, Mariano Esquillor s/n, 50018 Zaragoza, Spain*
[c]*Instituto de Nanociencia y Materiales de Aragon (INMA), CSIC-U. de Zaragoza, Calle Pedro Cerbuna 12, 50009 Zaragoza, Spain*
[d]*ARAID Foundation, 50018 Zaragoza, Spain*

† Electronic supplementary information (ESI) available: Additional spectra, STEM images, voltammograms and HER parameters. See https://doi.org/10.1039/d2se00218c

‡ Equally contributed to this work.

For example, growth of MoS_2 nanopatches on single-walled carbon nanotubes was recently found to promote efficiently the electrocatalysis of the HER,[11] as does a 2D/2D hetero-layered van der Waals architecture of MoS_2/graphene.[12] The stimulus, however, had been given earlier, with the growth of MoS_2 nanoparticles on reduced graphene oxide (RGO), as a reliable solution to improve the electrocatalytic performance of MoS_2 *via* hybridization with graphitic nanosheets,[6] and the promising HER results inspired other research groups to engage in this pairing.[13–16] RGO was also utilized to tune the electronic states of MoS_2 in MoS_2/RGO, and the effect of the latter on the HER was evaluated.[17] The HER electrocatalytic activity of MoS_2 has reportedly been boosted by interfacing nitrogen-doped RGO nanosheets,[18] while the coupling of MoS_2 hollow spheres with RGO towards the HER electrocatalysis and energy conversion applications has been also presented.[19] Recently, GO and RGO have been comparatively studied for the electrocatalysis of the HER in conjunction with MoS_2, and the MoS_2/GO heterostructure was found to be catalytically superior.[20] In a recent study, the excellent HER performance of MoS_2/GO was ascribed to the metallic 1T phase domains of MoS_2-based materials and strong interactions between the two counterparts, albeit the mechanisms taking place remain quite unclear.[21] However, all the aforementioned synthetic procedures involve the implementation of graphene derivatives and inorganic precursors of MoS_2 by solvothermal/hydrothermal methods, high-pressure autoclave methods and exposure to microwave irradiation. Consequently and as a significant handicap, these methodologies do not provide control over the morphology and chemical composition of the hybrids, especially those of MoS_2; therefore, there is limited insight not only regarding the chemical interaction of the counterparts, but also for the reasoning behind their synergism and thus the enhanced HER performance of the hybrids.

Yet, the different chemical structures of graphene oxide and exfoliated transition metal dichalcogenide nanosheets, that allow functionalization and introduction of specific functional groups, offer the tools for the design of heterostructures *via* specific and controlled covalent and non-covalent interactions. In this direction, we envisioned a rational approach for the construction of a novel layered MoS_2/graphene heterostructure for the electrocatalysis of the HER, employing the bifunctional polystyrene-*b*-poly(acrylic acid), PS-*b*-PAA, block copolymer as an interfacial modifier, adhering the two laminar nanostructures and allowing charge transport. More specifically, we herein present a covalent functionalization route accessing positively charged graphene oxide nanosheets to enable attractive electrostatic interactions with the anionic polycarboxylate PAA block of the copolymer, while on the other hand, multiple van der Waals S–π interactions between surface sulfur atoms of chemically exfoliated MoS_2 and the benzene rings of the PS block of the copolymer take place. This approach allows room-temperature processing of the MoS_2/graphene heterostructure in the solution phase without self-aggregation of the counterpart nanosheets. The newly derived heterostructure was extensively characterized *via* IR and Raman spectroscopies, thermogravimetric analysis (TGA), ζ-potential and dynamic light scattering (DLS) measurements, (scanning) transmission electron microscopy ((S)TEM) imaging and energy dispersive X-ray spectroscopy (EDS), and the electrocatalytic HER performance and durability of the as-prepared heterostructure were also examined.

Experimental

Instrumentation

Ultrasonication was performed with the aid of a Bandelin Sonoplus GM3200 equipped with a VS 70 T extended probe at 50% power (75 W, 20 kHz). UV-vis spectra were recorded on a PerkinElmer Lambda 19 UV-vis-NIR spectrophotometer, and the absorption of water was subtracted. ^{1}H NMR spectra were recorded using a Varian 300 MHz spectrometer. FT IR spectra were recorded on a Bruker Equinox 55 FTIR spectrometer equipped with a Pike Miracle Ge ATR accessory. Micro-Raman scattering measurements were performed at room temperature in the backscattering geometry using a RENISHAW inVia Raman microscope equipped with a CCD camera and a Leica microscope. 2400 lines per mm grating (for 514 nm) and 1200 lines per mm grating (for 633 nm) lasers were used, providing a spectral resolution of ± 1 cm^{-1}. As an excitation source, Ar (514 nm) and He/Ne lasers (633 nm) were used. Measurements were taken with 10 s of exposure time and laser power $\sim$0.3 mW cm^{-2} to prevent overheating and damage of the basal plane. The laser spot was focused on the sample surface using a long working distance 50$\times$ (L50) objective. Raman spectra were collected on numerous spots on the sample and recorded with a Peltier cooled CCD camera. For the Raman mapping recordings, 5–10 areas of 121 acquisition points (20 $\times$ 20 μm) each were scanned for every sample, and we present here a representative one close to the total average with respect to the intensity ratio I_D/I_G. The data were collected and analyzed with Renishaw Wire and Origin software. Dynamic light scattering (DLS) measurements were conducted on an ALV/CGS-3 compact goniometer system (ALVGmbH, Hessen, Germany), equipped with an ALV 5000/EPP multi-τ digital correlator with 288 channels and an ALV/LSE-5003 light scattering electronics unit for the stepper motor drive and limit switch control. A JDS Uniphase 22 mW He–Ne laser ($\lambda = 632.8$ nm) was used as the light source. The scattering intensity and correlation functions were measured at 90° angle. Correlation functions were collected and analyzed using the cumulant method and the CONTIN software, which provide the apparent hydrodynamic radius distributions by Laplace inversion of the correlation function and by aid of the Stokes–Einstein relationship. Zeta potential measurements were performed with a Zetasizer Nano ZS from Malvern Instruments (UK) equipped with a He–Ne laser (632.8 nm) and using a non-invasive back scatter (NIBS) technology. The zeta potential values were determined using the Smoluchowski equation relating the ionic mobilities with the surface charge and are reported as averages of ten repeated measurements. All electrochemical measurements were carried out using a Metrohm Autolab PGSTAT128N potentiostat/galvanostat at room temperature in a standard three-compartment electrochemical cell by using a graphite rod as a counter-electrode, an RDE with

a glassy carbon disk (geometric surface area: 0.196 cm^2) as a working electrode, and $Hg/HgSO_4$ (0.5 M K_2SO_4) (AMEL S.r.l., Milan, Italy) as a reference electrode. LSV measurements for the HER were carried out at room temperature in N_2-saturated 0.5 M H_2SO_4. A catalyst ink was prepared by dispersing 1.0 mg of the catalytic powder in a 250 μL mixture of water, isopropanol, and 5% Nafion (v/v/v = 4 : 1 : 0.02) and sonicated for 30 min prior to use. Before casting the electrocatalytic ink on the electrode's surface, the working electrode was polished with 6-, 3- and 1 mm diamond pastes and polishing alumina, rinsed with deionized water, and sonicated in double-distilled water. Afterwards, 8.5 μL aliquots of the electrocatalyst were cast on the electrode surface and were dried under a N_2 flow at room temperature. Electrochemical impedance spectroscopy (EIS) measurements (Metrohm Autolab, Utrecht, the Netherlands) were conducted from 10^5 to 10^{-1} Hz with an AC amplitude of 0.01 V, at a potential where significant HER was recorded, at −2 mA cm^{-2}. The EIS data were fitted to the Randles circuit. In the EIS fit and simulation, the Chi square value is <0.001. The data were obtained and analyzed with the Nova 2.1.4 software (Metrohm Autolab, Utrecht, the Netherlands). High-resolution transmission electron microscopy (HRTEM) imaging studies were performed on an image-corrected FEI Titan Cube microscope operating at 80 kV. Scanning transmission electron microscopy (STEM) and energy dispersive X-ray spectroscopy (EDS) analyses were performed on a probe-corrected FEI Titan-Low-Base 60–300 operating at 80 kV (equipped with an X-FEG® gun and Cs-probe corrector (CESCOR from CEOS GmbH)). For TEM analysis, the sample was dispersed in ethanol, and the suspension was ultrasonicated and dropped onto a copper carbon holey grid. The XPS data were acquired using a Kratos Axis Supra spectrometer equipped with a monochromated Al Kα X-ray source using an analyzer pass energy of 160 eV for the survey spectra and 20 eV for the core level spectra. Spectra were recorded by setting the instrument to the hybrid lens mode and the slot mode providing approximately a 700 × 300 μm^2 analysis area using charge neutralization. Regions were calibrated using the reference value BE (C 1s sp^2) = 284.5 eV. All XPS spectra were analyzed using CASA XPS software. The XPS peaks were fitted to a GL(70) Voigt lineshape (a combination of 70% Gaussian and 30% Lorentzian character), after performing a Shirley background subtraction.

Materials and methods

Reagents were purchased from Sigma-Aldrich and were used without further purification unless stated otherwise. Extreme care must be taken when working with *n*-BuLi, since it reacts violently with humidity/water and is pyrophoric. All procedures were performed in well-ventilated hoods.

Synthesis of *tert*-butyl (2-(2-(2-aminoethoxy)ethoxy)ethyl) carbamate (EDBEA-BOC)

The compound was synthesized based on published procedures[22,23] with modifications. To a solution of 2,2′-(ethylenedioxy)bis(ethylamine) (10 g, 68 mmol) in dichloromethane (50 mL), a solution of Boc_2O (1.47 g, 6.8 mmol) in dichloromethane (30 mL) was added dropwise over a period of 3 hours. The reaction mixture was stirred overnight at r.t. After this period, the reaction mixture was evaporated to 20 mL under reduced pressure and vacuum filtered through a P4 Büchner funnel to remove the unreacted Boc_2O solid. Then the reaction mixture was evaporated to dryness, redissolved in dichloromethane (20 mL) and washed twice with water. The organic layer was dried with Na_2SO_4 and evaporated to dryness. The residue was purified by flash chromatography (SiO_2, hexane : EtOAc 6 : 1). Yield: 96%.

Synthesis of the polystyrene macromolecular chain transfer agent (PS macro-CTA)

In a 25 mL round bottom flask, styrene monomer (2 g), 2-(dodecylthiocarbonothioylthio)-2-methylpropionic acid (0.182 g, 0.5 mmol), 2,2′-azobis(2-methylpropionitrile) (0.0082 g, 0.05 mmol) and 1,4-dioxane (6 mL) were added, and the oxygen was removed by bubbling high purity nitrogen for 15 min. Then, the flask was sealed and placed in a pre-heated oil bath (80 °C) and stirred for 12 h. After this period, the reaction mixture was initially cooled to −20 °C and then exposed to the atmosphere to terminate the radical polymerization. The reaction mixture was poured into a 10-fold excess of methanol to precipitate the polystyrene (PS) homopolymer (PS macro-CTA). Yield: 1.6 g.

The PS macro-CTA is of high purity and free of any monomer, as witnessed by ^1H NMR spectroscopy, and its molecular weight (M_w) was estimated through size exclusion chromatography to be 4.700 g mol^{-1} with a $M_w/M_n = 1.19$ (Fig. S1†).

Synthesis of the polystyrene-*block*-polyacrylic acid copolymer (PS-*b*-PAA)

First, the acrylic acid monomer was purified *via* a column packed with a resin in order to remove the *p*-methoxyphenol stabilizer. In a 25 mL round bottom flask, the acrylic acid monomer (0.45 g), the PS macro-CTA (0.376 g), 2,2′-azobis(2-methylpropionitrile) (0.003 g, 0.018 mmol) and 1,4-dioxane (6 mL) were added, and the oxygen was removed by bubbling high purity nitrogen for 15 min. Then, the flask was sealed and placed in a pre-heated oil bath (70 °C) and stirred for 15 h. After this period, the reaction mixture was initially cooled to −20 °C and then exposed to the atmosphere to terminate the radical polymerization. The reaction mixture was poured into a 10-fold excess of diethyl ether to precipitate the polystyrene PS-*b*-PAA copolymer, which was then placed in a vacuum oven to dry. Yield: 0.82 g.

The PS-*b*-PAA copolymer is of high purity, as witnessed by ^1H NMR spectroscopy (Fig. S2†). The PS : PAA ratio was also calculated *via* the ^1H NMR spectrum *via* the H3–H4 protons of PS and H9 protons of PAA, as depicted in Fig. S2.† Calculations are explained in the ESI† section.

Preparation of chemically exfoliated MoS_2 nanosheets (ce-MoS_2)

Initially, 750 mg (4.68 mmol) of bulk 2H–MoS_2 were placed in a furnace at 300 °C for 24 h. Then, the dried powder was placed

in a 25 mL flask with a magnetic stir bar and cooled to room temperature under a nitrogen atmosphere. Subsequently, 7.5 mL (18.75 mmol) of 2.5 M *n*-BuLi in hexanes were introduced, and the mixture was stirred vigorously for 48 h under nitrogen. After this period, the black suspension was left to settle, the intercalated solid Li_x-MoS_2 was precipitated and the supernatant *n*-BuLi solution was pipetted-off under nitrogen. Then 15 mL of dry hexane were introduced under nitrogen atmosphere, and the mixture was vigorously stirred for 10 minutes. Then, the as-formed black suspension was left to settle, the intercalated solid Li_x-MoS_2 was precipitated and the supernatant containing the excess *n*-BuLi was pipetted-off under nitrogen. This step was repeated two more times to ensure the removal of excess *n*-BuLi from the reaction mixture. The residual black slurry of Li_x-MoS_2 was opened in air and rapidly immersed in a 1 L flask filled with 750 mL of cold distilled water. Water reacts rapidly with the Li_x-MoS_2 evolving gas. The immersed flask and the stir bar were removed, and the mixture ($C = 1$ mg mL^{-1}) was ultrasonicated for 3 h (pulse ON: 3 s–OFF: 3 s), keeping the temperature below 30 °C with the aid of an ice bath. Finally, the suspension was left to settle overnight; the top 2/3 were collected and stored in a sealed flask in the dark and below 30 °C. The concentration of the ce-MoS_2 suspension was calculated as follows: 3 mL of the suspension were filtered through a pre-weight PTFE membrane filter under vacuum and washed with distilled water and ethanol, and the filter cake was dried under vacuum and weighted. Accordingly, the concentration of the suspension was calculated to be as high as 0.96 mg mL^{-1}.

Preparation of graphene oxide nanosheets (GO)

In a 500 mL round-bottom flask, a mixture of graphite powder (2 g, particle size <150 mesh) and concentrated sulfuric acid (12 mL) was stirred, and phosphorus pentoxide (2.5 g) was gradually added. Then, potassium persulfate (2.5 g) was added in small portions. The resulting mixture was placed in a pre-heated oil bath (80 °C) and stirred for 24 h. Subsequently, the mixture was cooled to r.t., diluted with 400 mL distilled water and vacuum filtered through a PTFE membrane (pore size 200 nm) filter. The collected solid was transferred into a 250 mL round-bottom flask immersed in an ice-bath. Nitric acid (30 mL) was added slowly under stirring, and then concentrated sulfuric acid (120 mL) was added in portions, keeping the mixture's temperature below 30 °C. Then, potassium permanganate (15 g) was gradually added to the mixture under stirring and left under stirring for 4 days at r.t. Finally, the mixture was transferred into a 2 L Erlenmeyer flask containing 1 L distilled water, and subsequently, hydrogen peroxide (20 mL 30% w/w solution) was introduced dropwise under stirring. Graphene oxide (GO) was collected *via* filtration of the mixture through a PTFE membrane (pore size 200 nm) filter. The solid (GO) was then washed with copious amounts of distilled water until the pH of the filtrate reached ≥5. GO was dried in a vacuum oven for 16 h. Yield: 1.62 g.

Preparation of GO-BOC nanosheets

In a 50 mL round-bottom flask equipped with a condenser and an inlet for nitrogen gas, GO (50 mg) and thionyl chloride (20 mL) were added and then heated in a pre-heated oil bath (75 °C) for 12 h under a nitrogen atmosphere. Then, the mixture was cooled down; the excess of thionyl chloride was removed under reduced pressure and kept under nitrogen. Dry THF (20 mL) was introduced into the flask, and the mixture was sonicated to wash the trapped excess of thionyl chloride. The mixture was dried under reduced pressure, and the residual solid was kept under nitrogen. A solution of EDBEA-BOC (0.3 g) and dry triethylamine (1 mL) in dry THF (25 mL) was added to the flask containing the thionyl chloride-treated nanosheets; a condenser with a nitrogen inlet was added, and the mixture was stirred under nitrogen in a pre-heated oil-bath (40 °C) for 3 days. Finally, the reaction mixture was dried under reduced pressure and dispersed in THF (75 mL) by sonication. The dispersion was filtered through a PTFE membrane (pore size 200 μm) filter and washed thoroughly with THF to collect the GO-BOC nanosheets as a black powder.

Preparation of positively charged modified graphene oxide nanosheets (GO^+)

In a 50 mL round-bottom flask, the GO-BOC from the previous step was dispersed in dichloromethane (30 mL), and trifluoroacetic acid (3 mL) was added. The mixture was left under stirring at r.t., and GO^+ nanosheet precipitation was immediately observed. The GO^+ nanosheets were collected *via* centrifugation (3000 rpm, 5 min), washed with 20 mL dichloromethane and dried under vacuum.

Preparation of the MoS_2/PS-*b*-PAA/GO^+ heterostructure

In a 25 mL flask, 10 mg of PS-*b*-PAA were dissolved in 1 mL DMSO followed by addition of an equimolar (with respect to the –COOH groups of PAA) amount of 0.1 M NaOH to promote the conversion of carboxylic acid groups to carboxylate anions. Then, it was diluted in 2 mL distilled water and was injected into a 3 mL dispersion of ce-MoS_2 (0.96 mg mL^{-1} concentration). The resulting ce-MoS_2/PS-*b*-PAA mixture was sealed and placed in a sonication bath for 1 h.

In a separate 10 mL flask, GO^+ nanosheets (3 mg) and 5 mL DMSO were added and placed in a sonication bath for 1 h. This suspension was added to the ce-MoS_2/PS-*b*-PAA mixture and was left under stirring for 3 days. The MoS_2/PS-*b*-PAA/GO^+ heterostructure was collected on a PTFE membrane filter (pore size = 500 nm) and washed with DMSO, distilled water and methanol to remove the excess copolymer. Finally, the heterostructure was dried in a vacuum chamber at r.t.

Ninhydrin (Kaiser) test

In a 10 mL centrifuge tube, GO^+ (1 mg), 75 μL phenol solution (1 g phenol in 2 mL ethanol), 100 μL KCN solution (0.2 mL aqueous 1 mM KCN in 9.8 mL pyridine) and 75 μL ninhydrin solution (100 mg ninhydrin in 2 mL ethanol) were added. The mixture was sonicated for 1 min and placed in a pre-heated oil bath (100 °C) for 7 minutes to promote the reaction between ninhydrin and the amines of GO^+. Then, the mixture was diluted with ethanol up to a total volume of 5 mL, sonicated for 1 min and centrifuged (4000 rpm, 1 min). A deep blue

supernatant validated the presence of amines in the sample (formation of Ruhemann's purple complex, positive test). The supernatant was placed in a UV-vis cuvette to record the absorbance of the blue complex (A_{max} = 570 nm) (Fig. S3†). In parallel, a blank sample without the GO^+ was also prepared. The calculation of amines *via* the UV-vis spectrum of the ninhydrin test was based on the following equation:[24]

$$\text{amine loading } (\mu\text{mol amine/gram } GO^+) = \frac{(\text{Abs}_{\text{sample}} - \text{Abs}_{\text{blank}}) \times \text{dilution (mL)} \times 10^6}{\text{extinction coefficient} \times \text{sample weight (mg)}}$$

The extinction coefficient of the chromophore complex = 15 000; $\text{Abs}_{\text{sample}} - \text{Abs}_{\text{blank}}$ = 1.94; dilution = 5 mL; sample weight = 1 mg.

Results and discussion

In order to prepare the MoS_2/graphene heterostructure, we synthesized positively charged modified graphene oxide nanosheets (GO^+), the bifunctional polystyrene-*block*-polyacrylic acid (PS-*b*-PAA) copolymer, and chemically exfoliated MoS_2 nanosheets (ce-MoS_2). Polystyrene-*b*-poly(acrylic acid) was selected as a bifunctional copolymer, specifically designed to interact (a) with the positively charged modified GO^+ nanosheets *via* attractive electrostatic forces through the ionized PAA block, forming negatively charged polyacrylate species and (b) with the ce-MoS_2 nanosheets *via* multiple van der Waals S–π interactions *via* the surface sulfur atoms of ce-MoS_2 and the phenyl rings of the PS block of the copolymer.

Initially, a simple 3-step synthetic route was employed to produce GO^+ nanosheets (Fig. 1a). First, graphene oxide, conventionally produced from graphite, was treated with thionyl chloride to promote the conversion of the carboxylic acid functionalities to the corresponding highly reactive acyl chlorides. Then, the *N-tert*-butoxycarbonyl-2,2′-(ethylenedioxy)bis-(ethylamine) chain, abbreviated as EDBEA-BOC,[22,23] was covalently attached *via* a condensation reaction, furnishing the GO-BOC derivative. Acidic hydrolysis of the BOC-protecting group afforded the target positively charged modified GO^+ nanosheets (Fig. 1a).

The functionalization process was complementary monitored *via* Fourier transform infrared spectroscopy (FT-IR), thermogravimetric analysis (TGA) and spatial Raman spectroscopy. Oxidation of graphite was evident in the FT-IR spectrum of GO, where a dominant carbonyl vibration mode (1722 cm^{-1}) of the generated carboxylic acid functionalities is observed (Fig. 1b). The incorporation of thermally unstable oxygen functionalities onto graphene was also probed during heating of the GO nanosheets under nitrogen, where a characteristic low-temperature thermal degradation occurs, in contrast to the thermally stable graphite starting material (Fig. 1c). Lattice defects across GO were also validated by the evolution of the D band in the Raman spectrum (Fig. 2a), being uniformly distributed in the sample, as revealed by spatial Raman mapping *via* calculating the D-to-G band intensity ratio, with an average value of 0.88 (Fig. 2b).

Noteworthily, heteroatom doping (oxygen functionalities) due to oxidation of graphene also affects the position of the G-band (27 cm^{-1} upshift). Having a uniform starting material, GO nanosheets, is essential to perform the designed chemical route towards the realization of positively charged GO^+ analogues; otherwise, covalent functionalization will be partial or uncontrolled. The covalent incorporation of the organic chains onto GO was validated both in the stage of being BOC-protected, as well as in the final positively charged species at GO^+. From the FT-IR spectrum of GO-BOC, we observe the carbonyl amide vibration mode at 1665 cm^{-1} and the N–H amide mode at 1519 cm^{-1}, as well as the carbamide carbonyl mode of the BOC group at 1700 cm^{-1}. Upon hydrolysis of GO-BOC towards GO^+, the carbamide mode vanishes, while the amide-related modes remain intact, manifesting not only the completion of the reaction but also the presence of the covalently attached organic chains in the final material (Fig. 1b). Thermogravimetric

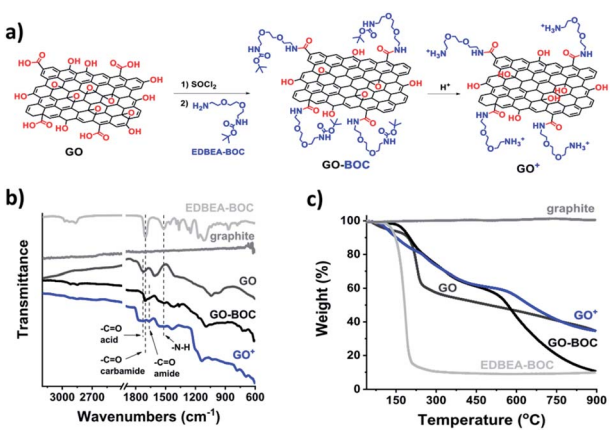

Fig. 1 (a) Chemical routes for preparing the positively charged GO^+ nanosheets. (b) FT IR spectra and (c) TGA graphs for GO (dark grey), GO-BOC (black) and GO^+ (blue), as well as reference graphite (grey) and EDBEA-BOC (light grey).

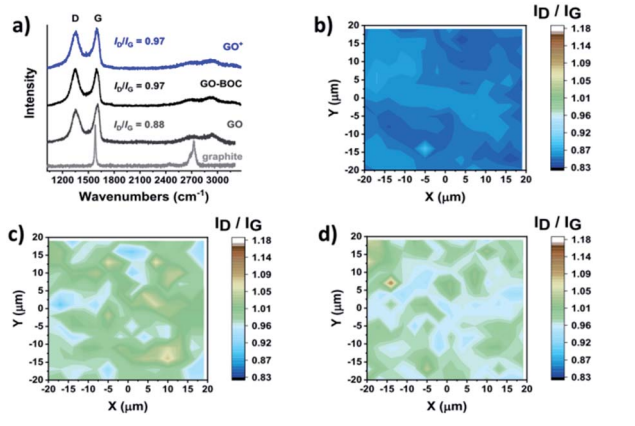

Fig. 2 (a) Raman spectra, at 514 nm excitation, for reference graphite (grey), GO (dark grey), GO-BOC (black) and GO^+ (blue) nanosheets. Spatial Raman mapping of the D/G intensity ratio at 514 nm, acquired in a 20 × 20 μm area (196 spots), for (b) GO, (c) GO-BOC and (d) GO^+ nanosheets.

analysis of GO-BOC and GO^+ sheds more light on the chemical process, in terms of the chemical functionalization, as well as the impact of the chemical treatment on the nanosheets. Fast thermal degradation of EDBEA-BOC is observed at ~200 °C, triggered by decomposition of the carbamide species (Fig. 1c). For both GO-BOC and GO^+, the organic chains were degraded at higher temperature, gaining thermal stability due to the presence of graphene. It is noteworthy that, during the activation of the carboxylic acid functionalities using thionyl chloride, mild temperature annealing was used (see experimental procedures for details). This is depicted in the TGA graph, showing a slightly better stability of GO-BOC and GO^+, and also in the Raman spectra. The D/G ratio for GO-BOC, as evidenced from the spatially collected spectra (Fig. 2c and d), is found increased (0.97), as compared to that of GO. Taking into consideration the employed amide-based chemistry, no further defects are expected in GO-BOC; thus, the D/G ratio should, in principle, remain constant. However, it is the use of the employed temperature in the chemical reaction, which initiated a healing process by partial degradation of the lattice, responsible for the witnessed increment of the D/G ratio in GO-BOC. Lattice healing is expected to increase the thermal stability of the nanosheets, which is evident for both GO-BOC and GO^+, as compared to GO. This is further validated by comparing the results from TGA and the D/G ratio in the Raman spectra between GO-BOC and GO^+. Hydrolysis of the BOC-protecting group is not expected to introduce defects in the graphene lattice, since the reaction proceeds at room temperature, and the chemistry occurs on the already covalently grafted organic chain. Actually, this was the case, and the D/G ratio in the Raman spectra is not altered as evidenced by the spatial Raman spectroscopy mapping of GO^+ (Fig. 2d). Finally, the presence of free amines on GO^+ was calculated *via* the ninhydrin (Kaiser) test[24] (see the Experimental section) and found to be as high as 647 μmol of amines per gram of GO^+ (Fig. S3†). Overall, the functionalization route towards GO^+ is straightforward, based on cheap reagents and can be easily monitored, furnishing highly uniform modified nanosheets. In parallel, styrene was polymerized *via* reversible addition fragmentation chain transfer (RAFT) polymerization and furnished polystyrene macromolecular chains, with a molecular weight of 4.700 g mol^{-1} and a polydispersity of 1.19, as evaluated by size exclusion chromatography (SEC). The PS was then used as a macro-chain transfer agent (macro-CTA) for the growth of the polyacrylic block. The composition of the PS-*b*-PAA copolymer was found to be 33% PS and 67% PAA, with a molecular weight of 11.300 g mol^{-1} and high purity. Treatment of PS-*b*-PAA with an equimolar (with respect to carboxylate groups of the PAA block) amount of sodium hydroxide enabled the ionization of PAA, the realization of the negatively charged polyacrylate block and its electrostatic interaction with the previously synthesized positively charged GO^+. Next, we focused on preparing ce-MoS_2 of high quality and high 1T phase content. Our approach relies on a simple protocol based on conventional laboratory apparatus, not requiring the use of a dry box.[25] A commercial semiconducting bulk MoS_2 powder was treated with *n*-butyl lithium under nitrogen, followed by removal of the excess organolithium reagent and tip sonication of the organolithium-intercalated MoS_2 material in distilled water. Accordingly, we managed to produce dispersions with a concentration of exfoliated nanosheets of up to 0.96 mg mL^{-1}, which are stable for over a month if stored in the absence of light and oxygen. Symmetry transition from the semiconducting hexagonal prismatic 2H to the metallic octahedral 1T occurred as a result of the chemical treatment. The latter was probed by UV-vis spectroscopy, where the freshly prepared ce-MoS_2 nanosheets lack the characteristic excitonic features of the semiconducting mode (Fig. S4†).[26] Phase transition is further illustrated in the recorded Raman spectra at 514 and 633 nm excitation, where the characteristic J phonon modes of the 1T symmetry at 151, 224 and 330 cm^{-1} appear for ce-MoS_2 (Fig. S5†). To promote the formation of the MoS_2/graphene heterostructure, freshly-prepared ce-MoS_2 aqueous suspensions were used in order to take advantage of the high stability of the nanosheets in aqueous media and the absence of aggregates. Tuning of the surface charges of GO^+ is essential to construct the heterostructure with MoS_2. Zeta (ζ) potential assays allowed us to estimate the charges present on the surface of graphene- and MoS_2-derived nanosheets. GO displayed a ζ potential value of −29.7 mV, which is expected as a result of the carboxylic acid functionalities. Further, ce-MoS_2 nanosheets also showed a negative ζ potential value of −29.1 mV, due to the chemical doping during the intercalation process. Evidently, these two materials are unlikely to form a heterostructure due to electrostatic repulsion. In contrast, the surface functionalization of GO towards the positively charged GO^+ resulted in a positive ζ potential value of +17.3 mV, unlocking the formation of a heterostructure with MoS_2 due to favorable electrostatic attraction. Herein, the role of the PS-*b*-PAA copolymer is to act as a bifunctional filler/linker, preventing the aggregation of the nanostructured counterparts and collapse due to the bulk nature of the nanosheets. In an alkaline environment, the ionized PAA block is capable to be immobilized on the surface of GO^+ *via* attractive electrostatic forces, while the PS block allows the development of S–π interactions between the sulphur atoms of MoS_2 and the aryl-rings of the styrene functionalities. Accordingly, the GO^+ and ce-MoS_2 counterparts could form layered superstructures, namely MoS_2/PS-*b*-PAA/GO^+ (Fig. 3a), where the PS-*b*-PAA macromolecules could potentially occupy the interlayer space. Dynamic light scattering (DLS) studies provided information on the lateral size of GO^+ and ce-MoS_2 (Fig. 3b). In more detail, the hydrodynamic radius of the ce-MoS_2 suspension was found to be 300 nm, with the corresponding value for GO^+ being 700 nm. The formation of the MoS_2/PS-*b*-PAA/GO^+ heterostructure was investigated by mixing ce-MoS_2 and GO^+ counterparts (1 : 1 mass ratio) in the presence of excess PS-*b*-PAA. Purification by vacuum membrane filtration was preferred, since removal of free PS-*b*-PAA and ce-MoS_2 nanosheets was manageable *via* controlling the pore size of the membrane filter. In particular, the small lateral size ce-MoS_2 nanosheets penetrate the membrane pores and are transferred to the filtrate, together with the excess PS-*b*-PAA, in contrast to the large lateral size GO^+ remaining on the filter surface. Mixing of GO^+, ce-MoS_2 and PS-*b*-PAA in the wet phase resulted in

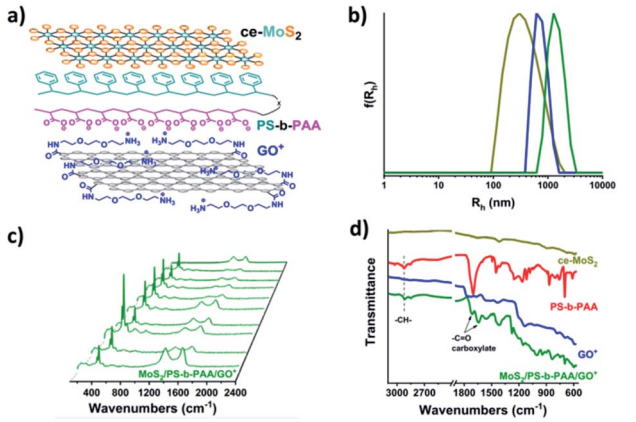

Fig. 3 (a) Illustration of the MoS_2/PS-*b*-PAA/GO^+ heterostructure. (b) DLS graphs for ce-MoS_2 (dark yellow), GO^+ (blue) and the MoS_2/PS-*b*-PAA/GO^+ heterostructure (green). Raman spectra at (c) 514 nm excitation for the MoS_2/PS-*b*-PAA/GO^+ heterostructure. The representative spectra acquired in a 20 × 20 μm area were used for the construction of the Raman graphs. (d) FT IR spectra for the PS-*b*-PAA copolymer (red), ce-MoS_2 (dark yellow), GO^+ (blue) and the MoS_2/PS-*b*-PAA/GO^+ heterostructure (green).

a uniform stable dispersion, and upon filtration, the isolation of the heterostructure, stabilized by PS-*b*-PAA, was achieved. Formation of the MoS_2/PS-*b*-PAA/GO^+ heterostructure increased the hydrodynamic radius up to 1400 nm as a result of the produced laminated superstructure (Fig. 3b). The ζ-potential value of MoS_2/PS-*b*-PAA/GO^+ was significantly decreased (−17.0 mV) as compared to those of the two counterparts, indicating strong attraction between them within the isolated heterostructure. In contrast, in a reference material composed of pristine GO, ce-MoS_2 and PS-*b*-PAA, we observed the formation of aggregates during mixing, and the ζ-potential value of the isolated material remained highly negative (−24.7 mV), suggesting electrostatic repulsion. This was further elaborated by evaluating the reference material *via* Raman spectroscopy. Raman modes originating from ce-MoS_2 were of low intensity, suggesting a non-uniform distribution of the nanosheets during mixing and isolation, implying the deficiency of GO to facilitate the formation of the heterostructure (Fig. S6†). The opposite is depicted in the Raman spectra (514 excitation) of the MoS_2/PS-*b*-PAA/GO^+ heterostructure (Fig. 3c), where more uniform distribution of the two materials within the heterostructure is evident, with both the Raman modes of ce-MoS_2 and GO^+ being intense. Noteworthily, the 1T phase of ce-MoS_2 was found to be stabilized, since the characteristic J phonon modes are evident in all recorded spectra. This could be related to a delocalization of the electron surplus of ce-MoS_2 (responsible for the 2H to 1T phase transition) over the PS block of the copolymer owing aryl units. Such a finding is of great importance with respect to the electrocatalytic properties of the heterostructure, since protection of the 1T phase is essential. In the FT-IR spectrum of MoS_2/PS-*b*-PAA/GO^+, the presence of PS-*b*-PAA in the anion (carboxylate) form is clearly observed (Fig. 3d).

Fig. 4a shows the HRTEM image of the MoS_2/PS-*b*-PAA/GO^+ heterostructure, showing the laminar nature of the structure with GO^+ nanosheets being covered with MoS_2 nanosheets. MoS_2/PS-*b*-PAA/GO^+ was further analyzed in detail by energy dispersive X-ray spectroscopy (EDS) in STEM. The heterostructure, composed of GO and MoS_2 flakes, is clearly observed in the micrographs and EDS maps (Fig. 4b). Furthermore, two other areas of this MoS_2/PS-*b*-PAA/GO^+ flake have been also analyzed; one is mostly composed of GO^+ (Fig. S7†), while in the second one, shown in Fig. S8,† MoS_2 is the main phase. The low

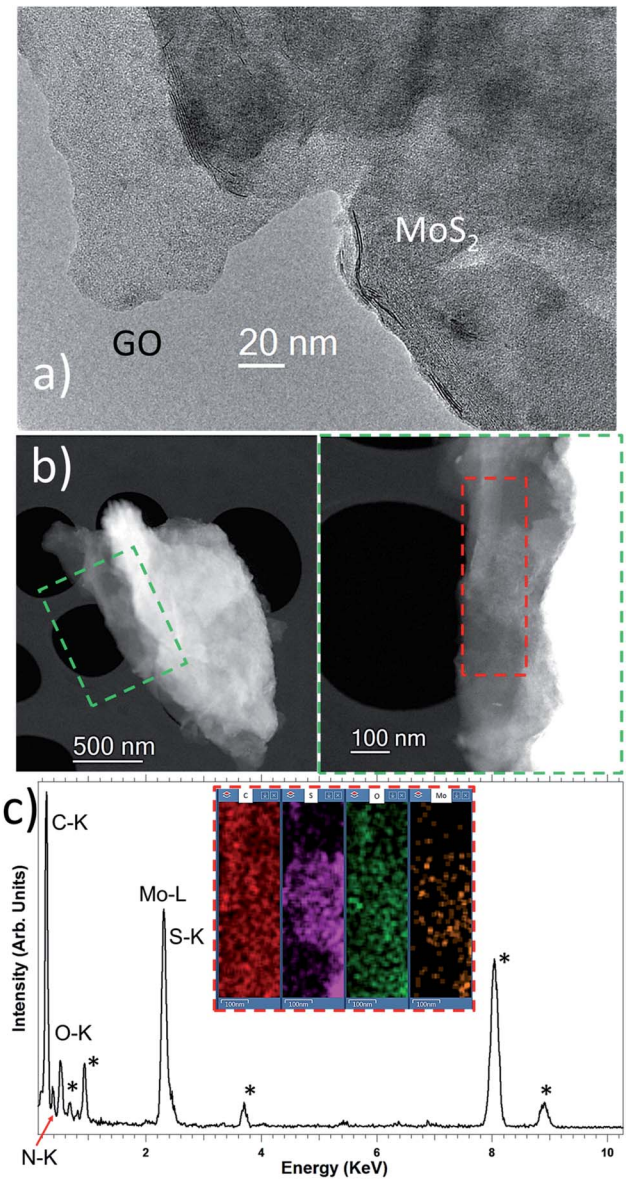

Fig. 4 (a) Imaging of the MoS_2/PS-*b*-PAA/GO^+ heterostructure by HRTEM. (b) Low-magnification (left panel) and high-magnification (right panel) high-angle annular dark-field (HAADF)-STEM images recorded for a flake composed of a MoS_2/PS-*b*-PAA/GO^+ heterostructure. The image on the right panel has been acquired in the green area highlighted on the left panel. (c) The EDS spectrum acquired in the red highlighted area of the image on the right panel. In the inset, the C, S, O and Mo elemental maps obtained from the analysis of this EDS spectrum-image are shown. Impurities due to F, Ca and Cu from the sample holder and grid are denoted as *.

magnification STEM image of MoS_2/PS-*b*-PAA/GO^+ is also shown in Fig. S9.†

In the XPS survey spectrum of MoS_2/PS-*b*-PAA/GO^+, characteristic peaks due to S 2p, C 1s, Mo 3p, N 1s, and O 1s located at binding energies of *ca.* 164, 285, 395, 400 and 533 eV, respectively, are evident (Fig. S10†). The C 1s, O 1s, Mo 3d and S 2p core-level spectra are also shown in Fig. S10.† The contributions of Mo^{4+} $3d_{5/2}$ and Mo^{4+} $3d_{3/2}$ correspond, as expected, to the 1T-MoS_2 phase.[27] Regarding the analysis of the C 1s spectrum, the peaks at ~284.5, ~286 and ~289 eV correspond to C–C, C=O, and COOH, respectively, as it can be observed in GO samples.[28]

Next, the electrocatalytic behavior of the heterostructure was evaluated for the HER *via* LSV assessments in aqueous 0.5 M H_2SO_4. We screened the optimum mass ratio of the ce-MoS_2 and GO^+ counterparts within the heterostructure with that of ce-MoS_2 and GO^+ counterparts with the 10 : 1 mass ratio being the best-performing and used for further evaluation of the electrocatalytic HER activity. Markedly, MoS_2/PS-*b*-PAA/GO^+ exhibited the lowest onset overpotential at −0.18 V *vs.* RHE, owing to 1T-MoS_2 immobilized on the GO^+ substrate, surpassing the electrocatalytic activity of both GO^+ and ce-MoS_2 reference materials (Fig. 5a). Furthermore, considering the functional current density required for sufficient hydrogen production at −10 mA cm^{-2}, at which misinterpretations from inherent electroactivity can also be prevented, the potential registered for MoS_2/PS-*b*-PAA/GO^+ is −0.31 V, which is positively shifted by 130 mV compared to that of ce-MoS_2 (*i.e.* −0.44 V) and by 370 mV compared to that of GO^+ (*i.e.* −0.68 V). For comparison, the polarization curve of commercially available 20 wt% Pt on carbon black (Pt/C), the supreme catalyst for the HER, is also presented in Fig. 5a.

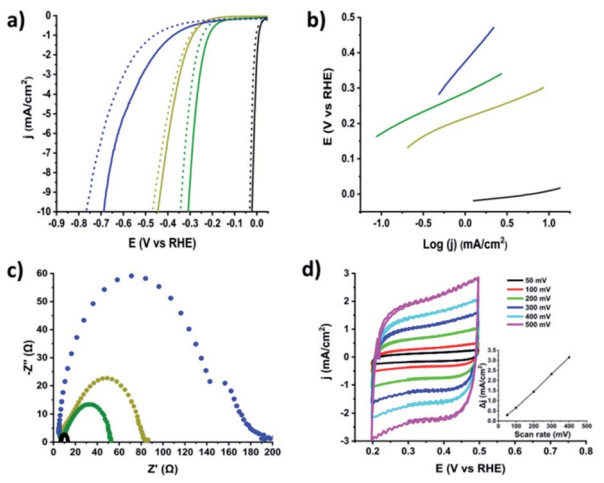

Fig. 5 (a) LSVs for the HER before (solid lines) and after 10 000 cycles (dashed lines); (b) Tafel slopes and (c) Nyquist plots of ce-MoS_2 (dark yellow), GO^+ nanosheets (blue), the MoS_2/PS-*b*-PAA/GO^+ heterostructure (green) and Pt/C (black). (d) Cyclic voltammograms (CVs) for the HER from 50–500 mV s^{-1} scan rates of MoS_2/PS-*b*-PAA/GO^+. Inset: scan rate dependence of the current densities for the corresponding materials. The LSVs and CVs were obtained at 1600 rpm rotation speed and 5 mV s^{-1} scan rate in N_2-saturated aqueous 0.5 M H_2SO_4, while the EIS measurements (Nyquist plots) were taken in the low overpotential (kinetic) region. The current densities are normalized to the geometric electrode area.

In the acidic-electrolyte-HER, the mechanism for electrocatalytic proton reduction and evolution of hydrogen is initiated by a primary discharge step (Volmer reaction) and is followed by either an electrochemical desorption (Heyrovsky reaction) or a recombination step (Tafel reaction). The discharge Volmer step involves the chemical incorporation of H into the catalyst by an oxonium ion and an electron association. During the Heyrovsky reaction, the H attached on the catalyst receives an electron from its surface and attacks a second oxonium ion to release gaseous H_2 and H_2O. Alternatively, H_2 is produced by direct association of two H attached on the surface, during the recombination step.[29] In order to determine which one of these steps is rate-limiting for the present electrocatalytic system, a Tafel post-experimental analysis was conducted. In Fig. 5b the Tafel slopes of MoS_2/PS-*b*-PAA/GO^+, ce-MoS_2, GO^+ and Pt/C, extracted from their respective LSV polarization curves, are depicted. The MoS_2/PS-*b*-PAA/GO^+ Tafel slope, which is 97 mV dec^{-1}, is greater than that of Pt/C (*i.e.* 30 mV dec^{-1}), but fairly lower than those of ce-MoS_2 (*i.e.* 114 mV dec^{-1}) and GO^+ (*i.e.* 283 mV dec^{-1}). Based on the calculated values, the HER of MoS_2/PS-*b*-PAA/GO^+ is governed by the Heyrovsky desorption.[30] The easier kinetics of the HER for the heterostructure, reflected by the low Tafel slope, reveal the accessibility and therefore reactivity of protons on the electrochemically active sites.

The HER kinetics were further assessed by electrochemical impedance spectroscopy (EIS), by which charge-transfer phenomena at the electrode/electrolyte interface under HER conditions were evaluated. The EIS measurements were performed in the low overpotential (kinetic) region, and the obtained data were fitted to the Randles circuit.[27] In more detail, the Nyquist plot of the MoS_2/PS-*b*-PAA/GO^+ heterostructure exhibited a charge transfer resistance (R_{ct}) as small as 36 Ω, more than twice lower compared to those of ce-MoS_2 (*i.e.* 69 Ω) and GO^+ (*i.e.* 146 Ω) and only 5 times higher than that of Pt/C (Fig. 5c). The smaller the diameter of the semicircle of the Nyquist plot, that correlates the electron transfer from the electrode surface into the electrolyte, the less the charge transfer resistance is. Thus, the decrement of the diameter of MoS_2/PS-*b*-PAA/GO^+, by almost 50% as compared to that of ce-MoS_2 and by 75% as compared to that of GO^+, further justifies the beneficial effect of combining the two nanosheets, highlighting the superior electrocatalytic activity of the heterostructure. The latter was further evaluated in a complementary manner, from the electrochemical surface area values (ECSA), that were calculated based on the cyclic voltammograms at different scan rates. In particular, whilst GO^+ is characterized by an extremely small (*i.e.* 13 cm^2) and inefficient ECSA (Fig. S11†), MoS_2/PS-*b*-PAA/GO^+ exhibits a higher ECSA value of 205 cm^2 (Fig. 5d), which is significantly greater than the ECSA of ce-MoS_2 (*i.e.* 123 cm^2) (Fig. S12†) and considerably closer to that of Pt/C (*i.e.* 362 cm^2) (Fig. S13†). Taking into account the calculated ECSA values for each material, the ECSA normalized LSV polarization curves are depicted in Fig. S14,† highlighting the intrinsic electrocatalytic activity of the MoS_2/PS-*b*-PAA/GO^+ material.

To conclude the electrocatalytic studies, the long-term stability of the MoS_2/PS-*b*-PAA/GO^+ heterostructure was evaluated *via* both durability assessments and a chronoamperometry measurement. Fig. 5a depicts the LSV polarization curves of ce-MoS_2, GO^+ and MoS_2/PS-*b*-PAA/GO^+ after 10 000 on-going catalytic cycles (dotted lines), where little overpotential increase is registered for the hybrid heterostructure (*i.e.* 12.5%). In order to highlight this important electrocatalytic aspect, we also recorded the chronoamperometric response of MoS_2/PS-*b*-PAA/GO^+ at a constant applied potential of −0.27 V *vs.* RHE in a time span of 10 000 s (Fig. S15a†). While the material was able to retain 65% of its original value after 10 000 s, we performed the complete electrocatalytic study afterwards to further validate this result. Interestingly, both the onset potential and the overpotential at −10 mA cm^{-2} shifted by only 10 mV (Fig. S15b†) (Table S1†). Likewise, the Tafel slope (Fig. S15b† inset) as low as 94 mV dec^{-1} was preserved. In contrast, the electrocatalytic activity loss upon recycling was evident from the EIS result, where the charge transfer resistance was found to be 38% higher (*i.e.* 59 Ω) than its initial (Fig. S15c†), but still lower than the respective ones of the reference materials (Table S1†). Finally, MoS_2/PS-*b*-PAA/GO^+ managed to retain more than 50% of its original ECSA after 10 000 s of use (Fig. S15d†).

Collectively, MoS_2/PS-*b*-PAA/GO^+ is an efficient electrocatalyst for the HER (Table S1†) owing to the synergistic effect of the two nanosheets/counterparts and to their unique chemical interactions. Graphene nanosheets provide high electrical conductivity and an increased surface area to not only facilitate the HER, but also to serve as a support matrix to MoS_2.[16] On the other hand, the high 1T-MoS_2 content in the MoS_2/PS-*b*-PAA/GO^+ heterostructure ensures a plethora of active sites and the reduced charge-transfer resistance.[7] In parallel, the chemical interaction between the two species prevents MoS_2 aggregation phenomena and facilitates the electron flow by creating a vast electroactive surface area, while the PS-*b*-PAA bridge locks the electrocatalytically active 1T phase of MoS_2.

Conclusions

In summary, we presented the design, preparation and complementary characterization of a MoS_2/graphene heterostructure, mediated by the bifunctional polystyrene-*b*-poly(-acrylic acid) copolymer. We demonstrated a straightforward covalent functionalization route for preparing modified graphene nanosheets bearing positively charged organic functionalities in a simple 3-step approach. The positively charged graphene oxide nanosheets (GO^+) carried an ammonium loading as high as 647 μmol g^{-1} of material, which proved to be sufficient to enable the solution-processed formation of the heterostructure, in contrast to non-modified graphene oxide. Within the laminar MoS_2/PS-*b*-PAA/GO^+ heterostructure, the polycarboxylate block of the PS-*b*-PAA copolymer was found to be in the anion form, while the octahedral symmetry (1T phase) of the ce-MoS_2 nanosheets was preserved. Our rational approach sheds light on the development of a MoS_2/graphene heterostructure, with precise chemical interactions of non-covalent character, emerging from the PS-*b*-PAA block copolymer interfacial modifier. As a proof of concept, the heterostructure was tested for the HER, where promising results were obtained reflected by a low onset overpotential of −0.18 V, a fairly small Tafel slope of 97 mV dec^{-1} and a charge transfer impedance of 36.2 Ω, as well as a vast surface area of 205 cm^2. The excellent HER performance of MoS_2/PS-*b*-PAA/GO^+ is attributed to the copolymer-assisted stabilization of the otherwise thermodynamically unstable 1T-MoS_2 that possesses a plethora of sulfur edges, which efficiently serve as catalytically active sites, for the efficient charge-transfer flow between GO and MoS_2, facilitated by the strategically selected PS-*b*-PAA bridge and their unique chemical interaction that also provides an increased surface area and prevents aggregation phenomena. Overall, it is a handy approach to improve the electrocatalytic performance of 1T-MoS_2 nanosheets and paves the way for future development of heterostructures with improved electrocatalytic activity.

Conflicts of interest

There are no conflicts to declare.

Acknowledgements

The TEM studies were performed in the Laboratorio de Microscopias Avanzadas (LMA), Universidad de Zaragoza (Spain). R.A. acknowledges support from the Spanish MICINN (PID2019-104739GB-100/AEI/10.13039/501100011033), Government of Aragon (projects DGA E13-20R (FEDER, EU)) and from EU H2020 "ESTEEM3" (Grant number 823717) and the Graphene Flagship (881603).

Notes and references

1 K. S. Novoselov, A. K. Geim, S. V. Morozov, D. Jiang, Y. Zhang, S. V. Dubonos, I. V. Grigorieva and A. A. Firsov, *Science*, 2004, **306**, 666–669.
2 A. Stergiou, R. Cantón-Vitoria, M. N. Psarrou, S. P. Economopoulos and N. Tagmatarchis, *Prog. Mater. Sci.*, 2020, **114**, 100683.
3 K. S. Rao, J. Senthilnathan, J.-M. Ting and M. Yoshimura, *Nanoscale*, 2014, **6**, 12758–12768.
4 X. Wang, S. M. Tabakman and H. Dai, *J. Am. Chem. Soc.*, 2008, **130**, 8152–8153.
5 H. Wang, L. F. Cui, Y. Yang, H. Sanchez Casalongue, J. T. Robinson, Y. Liang, Y. Cui and H. Dai, *J. Am. Chem. Soc.*, 2010, **132**, 13978–13980.
6 Y. Li, H. Wang, L. Xie, Y. Liang, G. Hong and H. Dai, *J. Am. Chem. Soc.*, 2011, **133**, 7296–7299.
7 M. A. Lukowski, A. S. Daniel, F. Meng, A. Forticaux, L. Li and S. Jin, *J. Am. Chem. Soc.*, 2013, **135**, 10274–10277.
8 S. Wang, D. Zhang, B. Li, C. Zhang, Z. Du, H. Yin, X. Bi and S. Yang, *Adv. Energy Mater.*, 2018, **8**, 1801345.
9 T. F. Jaramillo, K. P. Jorgensen, J. Bonde, J. H. Nielsen, S. Horch and I. Chorkendorff, *Science*, 2007, **317**, 100–102.

10 D. Voiry, M. Salehi, R. Silva, T. Fujita, M. Chen, T. Asefa, V. B. Shenoy, G. Eda and M. Chhowalla, *Nano Lett.*, 2013, **13**, 6222–6227.
11 Q. Liu, Q. Fang, W. Chu, Y. Wan, X. Li, W. Xu, M. Habib, S. Tao, Y. Zhou, D. Liu, T. Xiang, A. Khalil, X. Wu, M. Chhowalla, P. M. Ajayan and L. Song, *Chem. Mater.*, 2017, **29**, 4738–4744.
12 X. Yu, G. Zhao, S. Gong, C. Liu, C. Wu, P. Lyu, G. Maurin and N. Zhang, *ACS Appl. Mater. Interfaces*, 2020, **12**, 24777–24785.
13 E. G. Firmiano, M. A. Cordeiro, A. C. Rabelo, C. J. Dalmaschio, A. N. Pinheiro, E. C. Pereira and E. R. Leite, *Chem. Commun.*, 2012, **48**, 7687–7689.
14 C. B. Ma, X. Qi, B. Chen, S. Bao, Z. Yin, X. J. Wu, Z. Luo, J. Wei, H. L. Zhang and H. Zhang, *Nanoscale*, 2014, **6**, 5624–5629.
15 H. Li, K. Yu, C. Li, Z. Tang, B. Guo, X. Lei, H. Fu and Z. Zhu, *Sci. Rep.*, 2015, **5**, 18730.
16 H. Mao, X. Guo, Q. Fan, Y. Fu, H. Yang, D. Liu, S. Wu, Q. Wu and X.-M. Song, *Chem. Eng. J.*, 2021, **404**, 126253.
17 J. E. Lee, J. Jung, T. Y. Ko, S. Kim, S.-I. Kim, J. Nah, S. Ryu, K. T. Nam and M. H. Lee, *RSC Adv.*, 2017, **7**, 5480–5487.
18 Y.-J. Tang, Y. Wang, X.-L. Wang, S.-L. Li, W. Huang, L.-Z. Dong, C.-H. Liu, Y.-F. Li and Y.-Q. Lan, *Adv. Energy Mater.*, 2016, **6**, 1600116.
19 S. Kamila, B. Mohanty, A. K. Samantara, P. Guha, A. Ghosh, B. Jena, P. V. Satyam, B. K. Mishra and B. K. Jena, *Sci. Rep.*, 2017, **7**, 8378.
20 S. Kumar, P. K. Sahoo and A. K. Satpati, *ACS Omega*, 2017, **2**, 7532–7545.
21 Y. Lv, H. Pan, J. Lin, Z. Chen, Y. Li, H. Li, M. Shi, R. Yin and S. Zhu, *Chem. Eng. J.*, 2022, **428**, 132072.
22 R. B. Greenwald, H. Zhao, J. Xia, D. Wu, S. Nervi, S. F. Stinson, E. Majerova, C. Bramhal and D. W. Zaharevitz, *Bioconjugate Chem.*, 2004, **15**, 1076–1083.
23 G. Pastorin, W. Wu, S. Wieckowski, J. P. Briand, K. Kostarelos, M. Prato and A. Bianco, *Chem. Commun.*, 2006, **11**, 1182–1184.
24 C. Menard-Moyon, C. Fabbro, M. Prato and A. Bianco, *Chem.–Eur. J.*, 2011, **17**, 3222–3227.
25 A. Stergiou, C. Stangel, R. Canton-Vitoria, R. Kitaura and N. Tagmatarchis, *Nanoscale*, 2021, **13**, 8948–8957.
26 E. P. Nguyen, B. J. Carey, T. Daeneke, J. Z. Ou, K. Latham, S. Zhuiykov and K. Kalantar-zadeh, *Chem. Mater.*, 2014, **27**, 53–59.
27 A. Kagkoura, R. Arenal and N. Tagmatarchis, *Adv. Funct. Mater.*, 2021, **31**, 2105287.
28 S. Hettler, D. Sebastian, M. Pelaez-Fernandez, A. M. Benito, W. K. Maser and R. Arenal, *2D Materials*, 2021, **8**, 031001.
29 B. E. Conway and B. V. Tilak, *Electrochim. Acta*, 2002, **47**, 3571–3594.
30 T. Shinagawa, A. T. Garcia-Esparza and K. Takanabe, *Sci. Rep.*, 2015, **5**, 13801.